Influence of Substitution on the Structure and Electrochemistry of Layered Manganese Oxides

Tom A. Eriksson,[*,§] Young Joo Lee,[†] Joel Hollingsworth,[*] Jeffrey A. Reimer,[†] Elton J. Cairns,[†] Xiao-feng Zhang,[*] and Marca M. Doeff[*]

[*]Materials Sciences Division

and

[†]Environmental Energy Technologies Division

Lawrence Berkeley National Laboratory

University of California

Berkeley, CA 94720, USA

Acknowledgments

This work was supported by the Assistant Secretary for Energy Efficiency and Renewable Energy, Office of FreedomCAR and Vehicle Technologies of the U.S. Department of Energy under Contract No. DE-AC03-76SF00098. T.A. Eriksson was funded by The Hans Werthen Foundation and The American-Scandinavian Foundation.

[§]Present address: St. Jude Medical ABVeddestavagen 19SE-175 84 Jarfalla, Sweden

Abstract

Layered substituted lithium manganese oxides were prepared by ion-exchange of compounds with the nominal composition $Na_{0.7}MnO_2$ or $Na_{0.7}Mn_{0.89}M_{0.11}O_2$, (where M=Fe, Co, Ni, Cu, Zn, Li or Al) and were characterized structurally and electrochemically. The sodium-containing materials have P2 stacking or are P2/P3 intergrowths, whereas the lithiated analogs have O2 or stacking faulted O2/O3 structures. Compounds with O3 components exhibit higher capacity (or faster intercalation kinetics) than the pure O2 materials. Neither O2 nor, surprisingly, O2/O3 structures converted to spinel upon repeated charging in lithium cells to high voltages, for sixty or more cycles. The results presented herein suggest that it might be possible to design an electrode with an acceptable compromise between the phase stability of the O2 structure and the higher capacity (or better rate capability) of O3 compounds by manipulating the relative amounts and distributions of these two phases in intergrowth structures.

I. Introduction

To reduce the cost and improve the safety of Li-ion batteries for vehicular applications, new cathode materials are needed in place of the expensive and toxic lithium cobalt oxide systems currently used.[1,2] Manganese oxides are especially attractive from this perspective. However, spinel lithium manganese oxides exhibit poor cycling behavior at elevated temperatures and somewhat low capacity. [3,4] The manganese oxides are polymorphous, and either tunnel-containing or layered structures can be made depending upon reaction conditions and the presence or absence of other components (such as alkali metal ions). Layered materials, in particular, are interesting as cathode

materials because of the potential for high capacities. [5,6] $LiMnO_2$ with the α-$NaMnO_2$ structure and substituted variants, made by ion-exchange, transform into spinel upon electrochemical cycling, however.[7,8] In these materials, which usually have a monoclinic distortion due to the large number of Jahn-Teller Mn^{3+} ions (space group C2/m), lithium is located in octahedral sites, and there are three MO_2 layers per unit cell. In layer notation, this is designated O'3 (Figure 1a). The oxygen anions in O'3 and O3 layered manganese oxides (Figure 1e) are in a nearly cubic close-packed array as in spinel, so that only minor rearrangements of Li and Mn ions are necessary for conversion to occur.

Recently, a layered lithium manganese oxide with a different stacking sequence has been reported to cycle stably in lithium cells.[9,10] This is made from a non-stoichiometric layered sodium manganese oxide, $Na_{0.7}MnO_{2+y}$, in which sodium ions reside in trigonal prismatic sites and there are only two MnO_2 layers per unit cell (P2 in layer notation, space group $P6_3mmc$), as shown in Figure 1b. Upon ion exchange, the transition metal layers glide to form octahedral (or in some cases, tetrahedral) sites for lithium in the van der Waal's gaps, forming O2, O6, or T2 structures.[11, 12] The O2 structure (space group $P6_3mc$) is shown in Figure 1c. The oxygen array is not cubic close-packed, implying that more bond-breaking and rearrangement is needed to form spinel, accounting for the better cycling stability.

The electrochemical properties of the O2 materials vary depending upon the type and degree of substitution of manganese ions. For example, all of the Li in $Li_{2/3}[Co_{1/3}Mn_{2/3}]O_2$ can be removed in the first charge cycle,[13] whereas only 1/3 of the Li can be removed from $Li_{2/3}[Ni_{1/3}Mn_{2/3}]O_2$.[14] To investigate the characteristics of these materials further, we prepared a series of O2 layered manganese oxides, wherein the

substituents were first-row transition-metals, lithium, or p-elements. An ultimate goal is to prepare electrodes with both high capacities and good cycling behavior. Herein, we report results on these compounds.

II. Experimental Procedures

Glycine-nitrate combustion synthesis was used to produce the precursor P2 $Na_{0.7}M_xMn_{1-x}O_{2+y}$ (where M is a metal substituent) or $Na_{0.7}MnO_{2+y}$ compounds. [15,16] $NaNO_3$, $Mn(NO_3)_2$ in HNO_3 and substituent metal-nitrate (e.g. $Ni(NO_3)_3 \cdot 6H_2O$), in proportions to give $Na_{0.7}M_{0.11}Mn_{0.89}O_{2+y}$ were mixed with glycine in the molar ratio 1:2 (glycine:nitrate) and diluted with de-ionized water. The temperature of the combustion reaction is determined by the glycine:nitrate ratio and was chosen to give 1300-1400°C. The solution was combusted by evaporating small aliquots of solution to dryness until the desired amount of product was obtained. The as-prepared powder was then calcined at 800°C for 4h to remove any organic residue and to ensure homogeneity.

For the ion exchange, the materials were refluxed in a solution of LiBr in ethanol (9 fold excess of Li) for 48h at 80°C, as described by Bruce et al. [7, 17] For most of the compounds, this was sufficient to remove all sodium-containing phases detected by xrd except for the unsubstituted material and that substituted with Cu. For the latter, an additional reflux was carried out using a solution of LiBr in hexanol (9 fold excess of Li) for 8h at 160°C to complete the reaction. In the case of the unsubstituted material, additional refluxing in hexanol caused decomposition, and further exchange did not occur when the reflux in ethanol was prolonged beyond 48h. All materials were carefully

washed in ethanol several times to remove any traces of salt residues and dried at 150 ºC for 24-48h to remove water.

Elemental compositions were determined by inductively coupled plasma (ICP) analysis (by Desert Analytics Laboratory, Tucson, AZ). X-ray powder diffraction (XRD) measurements were carried out on a Siemens 5000D diffractometer, with monochromized Cu radiation (λ = 1.54 Å). The program Fullprof was used for Rietveld refinements of the XRD patterns and Powdercell 2.3 for Windows used to generate the simulated patterns. Using Fullprof, the overall scale factor, half-width (U, V, W), cell parameters, zero-point, temperature factors (B), and oxygen z-value were refined. A pseudo-Voigt function was used. The R_B value was typically 15-20% depending on the "tailing" of peaks, due to intergrowths, as described in the structural characterization below. Particle morphologies were investigated with a Microspec ISI-DS 130C scanning electron microscope (SEM).

^{7}Li MAS NMR experiments were performed at 25.52 MHz on a home built spectrometer with a Doty probe equipped with 4 mm rotors for MAS. Spectra were obtained with a rotor-synchronized Hahn echo pulse sequence with evolution periods being chosen as one rotor period. A 90° pulse of 1.1 μs was used with a 2 s recycle delay. The spinning speeds were 22-23 kHz. All shifts were referenced to 1 M LiCl (aq.) solution, at 0 ppm. The ^{7}Li longitudinal relaxation times (T_1) were measured with an inversion-recovery pulse sequence combined with a Hahn-echo sequence to avoid a distortion caused by the spectrometer dead time.

For transmission electron microscopy (TEM) examination, $Na_{0.63}Mn_{0.89}Al_{0.11}O_{2.05}$ powder was suspended on carbon holey films on Cu grids. TEM characterization was

performed in a 200 kV field-emission-gun Philips CM200 transmission electron microscope at the National Center for Electron Microscopy (NCEM), at the Lawrence Berkeley National Laboratory.

Electrodes were prepared by thoroughly mixing active material with carbon black (Shawinigan black), SFG-6 graphite (Timrex Timcal) and polyvinylidene fluoride (PVdF, Kynar 7140) in N-methyl-pyrrolidinone and extruding onto an aluminum-foil. The final composition of the electrodes was 80 wt% active material, 6% carbon black, 6% graphite, and 8% PVdF. The electrodes were allowed to dry over night at room temperature and then for 24h at 120°C under vacuum. Coin cells were assembled in a glove-box (<1 ppm O_2/H_2O) using Celgard 3401 as the separator, 1:2 ethylene-carbonate (EC)/dimethyl-carbonate (DMC) + 1M $LiPF_6$ electrolyte (Selectipur®, Merck, Darmstadt, Germany) as the electrolyte solution, and Li-foil (Cyprus-Foote Mineral Co., Kings Mountain, NC) as the counter electrode. Cells were cycled between 4.6 V or 4.2 V and 2.0 V at a current density of 0.05 mA/cm^2. For ^{7}Li-MAS NMR measurements on electrodes as a function of charge, cells were subjected to one cycle and then taper-charged or discharged prior to analysis (i.e., constant-current charging or discharging was carried out to a voltage cutoff, cells were allowed to rest for 5 minutes and the desired constant potential was applied until the current decreased to $\pm 1 \times 10^{-6}$ mA). All electrochemical measurements were performed on an Arbin BT/HSP-2043 cycler or a MacPile II (Bio-Logic, SA, Claix, France) potentiostat/galvanostat.

III. Results and Discussion

Structural characterization. The chemical analysis of the substituted sodium-containing precursors yielded a molar ratio of 0.6Na:0.1M:0.85Mn (where M = Fe, Co, Ni, Cu, Zn, or Al). Density measurements in the original work[18] show that y is about 0.05 for hexagonal P2 phases, Na_xMnO_{2+y}, where x is about 0.7 (i.e., there are cation vacancies in the MO_2 layers). The compositions can thus be written as $Na_{0.6}[M_{0.1}Mn_{0.85}\square_{0.05}]O_2$ or $Na_{0.63}Mn_{0.89}M_{0.11}O_{2.05}$. Particles of all substituted compounds consisted of small crystallites, about 1-4 μm across, which are slightly fused together from the calcination, into larger agglomerates of 15-30 μm (Figure 2).

XRD patterns of the unsubstituted and substituted $Na_{0.63}Mn_{0.89}M_{0.11}O_{2.05}$ compounds are shown in Figure 3. Also included is a pattern calculated for $Na_{0.66}Ni_{0.33}Mn_{0.67}O_2$ from data reported by Dahn et al.[9] All compounds have predominantly the P2 layered structure, but several additional peaks were observed at medium angles in some of the patterns (Figure 4). These could be indexed to a P3 structure (space group R3M) similar to that reported recently by Bruce et al,[19] in which there are three MO_2 per unit cell, and trigonal prismatic sites for Na (Figure 1d). No superstructure peaks were detected in these patterns suggesting that there is an absence of ordering on the transition-metal sites. [12,20]

Interestingly, the 003 peak of the P3 constituent at low angles always coincided exactly with the 002 peak of the main P2 phase in compounds having both components. Peak broadening was also evident in these patterns, particularly in that of $Na_{0.63}Mn_{0.89}Al_{0.11}O_{2.05}$, which appeared to contain the most P3 phase. Additionally, attempts at full Rietveld refinements were unsatisfactory, due to "tailing" of peaks. These

observations suggest that the two phases are present as intergrowths rather than as separate materials. A transmission electron micrograph and electron diffraction pattern of $Na_{0.63}Mn_{0.89}Al_{0.11}O_{2.05}$ (Figure 5) confirm this. Fig. 5a shows a typical dual-phase grain with a "sandwich" arrangement of P2 and P3 phase slabs (i.e., zone intergrowths). The P2 slab is usually thicker than the P3 slab. This type of configuration was observed in about 40 % of the grains examined. Fig. 5b shows a corresponding selected-area electron diffraction pattern taken from the "sandwich" area. Diffraction patterns arising from both P2 and P3 phases are superimposed. Since the $(0002n)_{P2}$ and $(0003n)_{P3}$ (n is integer, subscripts denote P2 and P3 phase, respectively) are superimposed upon each other, only one set of (*000l*)* diffraction spots can be seen in Fig. 5b. Nevertheless, other diffraction rows from P2 and P3 phases, respectively, can also be recognized as indicated in Fig. 5b. Orientation relationships between the two phases can therefore be determined to be $[10\bar{1}0]^*_{P2}$ // $[10\bar{1}0]^*_{P3}$, and $(0001)_{P2}$ // $(0001)_{P3}$, with the interface plane between the P2 and P3 slabs parallel to the common (0001) planes. In addition to the dual-phase grains, single-phase grains were also observed: there were approximately four times as many P2 grains as P3 grains.

Recent work in our laboratory indicates that the relative amounts of P2 and P3 components in the intergrowths can be controlled by varying the Na:transition metal (Na:TM) ratio in the nitrate mixture prior to combustion, in some cases.[21] Very small changes in sodium content (e.g., ΔNa:TM $\approx$ 0.05), however, lead to large variations. Pure crystalline P3 compounds with an approximate composition of $Na_{0.5}Mn_xM_{1-x}O_2$ can be prepared at 800 ºC for at least some formulations. It appears, however, to be more

difficult or perhaps impossible to prepare pure P2 phases of several of the substituted materials (e.g., Ni or Al) by the glycine-nitrate combustion method.

Water may be intercalated in the van der Waal's gaps of these compounds,[22] and evidence of this was found in the xrd patterns of some of the samples (Fig. 6). Small peaks at about d = 7.00 Å (2θ = 12.7º) and d = 3.50 Å (2θ = 25.6º), especially prominent in Zn and Co-substituted samples, disappeared when the samples were thoroughly dried. These can be assigned to the (002) and (004) reflections of a hydrate phase with a c parameter increased by about 2.73 Å compared to the dried products.

Table 1 lists unit cell parameters of the P2 and P3 components of the $Na_{0.63}Mn_{0.89}M_{0.11}O_{2.05}$ compounds. The relationship between the ionic radius of M and the in-plane parameters, a, vary in a complex way (Table 2). Aliovalent substitution with larger ions sometimes results in a bigger unit cell (Zn^{2+}), but not always (Li^{+}), due to the increase in the relative amount of smaller Mn^{4+} ions, which offsets the effect of the substituting ion. Replacement of Mn^{3+} with smaller Al^{3+} ions (Table 2) does, however, cause the expected decrease in a. The larger unit cell parameters observed in $Na_{0.63}Mn_{0.89}Fe_{0.11}O_{2.05}$ suggest that Fe is in the divalent state.

Figure 7 shows the xrd patterns of the substituted layered compounds after ion-exchange, as well as calculated patterns for O2 Li_xMnO_{2+y} and O3 Li_xMnO_2 taken from atom positions reported in the literature.[19, 23] For most of the samples, no traces of the P2 sodium-containing precursor phases were observed. (In the Ni and Co-substituted compounds, small peaks attributable to hydrate phases are evident at 2θ=12.75 (d=6.9)). In the case of the Cu-substituted material, a peak at about 2θ = 16º indicates that the P2 phase is still present and the exchange was incomplete, even after an additional reflux in

hexanol. Full exchange was also not possible for the unsubstituted material (not shown), which decomposed when an additional reflux at higher temperatures was attempted. ICP analysis of the ion-exchanged materials indicated about 90% of the sodium was replaced by lithium for compounds with no P2 phase present. It is not currently clear whether the residual sodium is present on the surfaces of the particles as a contaminant or in the van der Waal's gaps. For the sake of simplicity, we will refer to these compounds as $Li_xM_{0.11}Mn_{0.89}O_{2.05}$ hereafter.

The ion exchange induces a shift in the transition metal layers so that octahedral sites for Li ions are formed. The major P2 component is converted to lithium-containing O2, whereas the minor P3 component converts to O3 (space group $R\bar{3}M$). The latter is similar to the O'3 structure shown in Figure 1a except that the monoclinic distortion is removed because of the higher average oxidation state of the Mn (i.e., there are fewer Jahn-Teller Mn^{3+} ions). No peak at 66º (d= 1.416), attributable to the (111) reflection of a T2 structure is observed in the patterns of any of the compounds. Lu et al have noted a relationship between the T2 structure and a superlattice in the substituted lithiated compounds, [20] which is absent in these materials.

There are both broad and narrow peaks in the diffractograms of the exchanged compounds, and a variation in intensity (some reflections are stronger while others have a lower intensity than expected). The (002) and (110) reflections are particularly sharp and high in intensity and the (h0l) reflections are broad and weak. This indicates the presence of stacking faults, another reason why it is so difficult to carry out full Rietveld refinements of these patterns with acceptable statistics. Transition metal substituents appear to influence the lattice parameters in the same way as in the sodium-containing

precursors (Table 3), and lithium substitution decreases c due to its smaller size relative to sodium.

To better understand the local structure around the Li-ions in the ion-exchanged materials, solid-state ^{7}Li MAS NMR spectra were collected. As shown in Figure 8 (a)-(f), $Li_xM_{0.11}Mn_{0.89}O_{2.05}$ show several resonances depending on the substituent metal. A dominant broad resonance at approximately 700 ppm and a sharp resonance at –5 ppm were observed for all the compounds. Additional resonances were seen at ~110 ppm for Ni, Co, Fe, and Al-substituted materials and at 300 ppm for the Cu-substituted compound. It appears that the NMR spectrum of the Zn-substituted compound does not contain an additional resonance. It was previously shown that the NMR spectra of lithium manganese oxides and lithium nickel oxides are dominated by the Fermi-contact interaction mediated by the intervening bonds.[24,25,26] The Li NMR shifts depend on the sum of the contribution of each Li–O–Mn (or, Ni) and the types of orbital involved. Taking the same postulate, the local environments of Li in O2 and T2-type structures were examined, and the hyperfine shifts were estimated. A shift of 270~430 ppm is predicted for Li in the tetrahedral site of a T2 structure and a shift of 940~1160 ppm for Li in the octahedral site of an O2 structure (the details of the Fermi-contact interaction will be discussed elsewhere). Thus, the resonances at 700 ppm and 300 ppm were tentatively assigned to the lithium cations in the O2-type environment and T2-type environment, respectively. Previously, a resonance at 133 ppm was obtained for O3-type layered manganese oxides.[27] Therefore, the resonance at 100-124 ppm is attributed to an O3-type environment. Since NMR is a quantitative technique, the content of the lithium cations in each environment can be estimated from the intensities of the resonances. The

Fe-substituted material contains a relatively small amount of O3-type Li, compared to the Ni, Co, and Al-substituted materials. This observation is consistent with the XRD patterns of unsubstituted $Na_{0.63}M_{0.11}Mn_{0.89}O_{2.05}$, which exhibit additional Bragg reflections corresponding to the P3 structure for Ni, Co, and Al-substituted compounds. This result suggests that the O3 phase is formed by the ion-exchange of Li into the P3 environments. The lack of the additional Bragg reflections corresponding to the P3 structure in Fe-substituted material is probably due to the small content of this phase below the XRD detection limit.

The longitudinal relaxation times, T_1, were measured for each resonance. T_1 values of 1.9, 1.5, 2.8 ms and 1.5 s were obtained for the resonances at 700, 300, 100, and –5 ppm, respectively. The presence of a paramagnetic species markedly decreases the relaxation time T_1, which is a function of magnetic moment, temperature, and the extent of the orbital overlap between a paramagnetic center and a nucleus. Thus, the short value of T_1 indicates that the lithium cations, which give rise to the resonances at 700, 300, and 100 ppm, are strongly coupled to Mn. In contrast, the relatively long T_1 associated with the -5 ppm peak indicates that the interaction between the Li and Mn cations is weak, suggesting that some lithium cations are residing on the surface of the grain. The relative intensity ratio of the resonances at 700, 100, and 0 ppm for $Li_xM_{0.11}Mn_{0.89}O_{2.05}$ was approximated as 25:1:4. No attempt was made to take into account the changes in relative intensity that may occur due to different T_2 relaxation times. Nonetheless, the value for the surface Li content of 13%, obtained by the sum of the intensity of the resonance at –5 ppm and the two 1st spinning sidebands, agrees well with the ICP elemental analysis. The surface lithium will not be involved in the electrochemical redox

reaction. The Cu-doped material contains 3-4 times the amount of surface Li as compared to the other compounds, consistent with the difficulty in the ion-exchange. The resonances for the surface, O3, and T2 Li show a narrow linewidth, whereas the resonance for Li in the O2 environment is the overlap of several resonances. We surmise that the existence of the fine structure is due to a distribution in the local environments surrounding O2 Li, suggesting an absence of ordering between Mn and the substituted metal ion. A narrow single resonance has been observed for $LiMn_{1.5}M_{0.5}O_4$ spinel (M=Ni, Zn) with 3:1 ordering between the Mn and M ions in the octahedral site.[28, 29] To check for the presence of the lithium cations in the layer occupied by the manganese ions (TM layer), the ^{7}Li NMR spectrum of $Na_yLi_{0.11}Mn_{0.89}O_{2.05}$ was acquired (Figure 8 (g)). A distinctive resonance at 1836 ppm is obtained for the Li cations in the TM layer. However, a resonance in this high frequency region is not seen in $Li_xM_{0.11}Mn_{0.89}O_{2.05}$, indicating that there is no cation mixing between Li and Mn in the transition metal layer.

Electrochemistry and post-mortem analysis. As-assembled, the Li/1M $LiPF_6$, EC-DMC/$Li_xM_{0.11}Mn_{0.89}O_{2.05}$ cells are in the partially discharged state, and may either be charged or discharged initially. The main redox reaction is a diffusion-controlled process centered at about 3.1 V.[30] Potential profiles of fully-charged cells discharged at 0.05 mA/cm^2 between 4.3 or 4.6 and 2.0 V are shown in Figures 9 and 10 and are generally sloping and featureless, indicative of single phase behavior. For most of the electrodes, the slope of the voltage profile steepens markedly above about 3.5 V, making it impossible to remove all the alkali metal ions even when cells are charged to 4.6 V.

The capacities obtained vary considerably with the nature of the substituents, ranging from about 80 mAh/g when M = Mn or Cu to about 150 mAh/g when M = Co or

Ni. For some poorer performing electrodes, e.g., when M = Fe (Figure 11), significantly higher utilization was obtained when the current density was decreased, suggesting kinetic limitations. Less severe limitations are observed for $Li_xM_{0.11}Mn_{0.89}O_{2.05}$ (M = Al, Ni) electrodes, although these also yield somewhat lower capacities galvanostatically than during slow stepped potential experiments (180 mAh/g between 3.9 and 2.0 V). [30]

Higher discharge capacities and/or better rate capabilities correlate strongly with significant presence of an O3 component in the layered structures (cells shown in Figure 10). A 100% O3 $Li_xNi_{0.2}Mn_{0.8}O_2$ electrode gives over 200 mAh/g in a lithium cell configuration and nearly all the alkali metal cations can be removed, but charge capacities decline as the amount of O2 component in O2/O3 intergrowths increases,[21] confirming this association. This suggests that Li diffusion is faster in layers with an O3 arrangement than in those with an O2 arrangement. It is not, at present, clear why this should be so, although perhaps differing numbers of vacancies in the MO_2 layers, which can trap lithium ions, may account for the dissimilarity.

Discharge curves for $Li_xM_{0.11}Mn_{0.89}O_{2.05}$ electrodes do not significantly change shape as cells are cycled, as is seen in Figures 9 and 10, although some capacity fading is seen. This suggests that spinel conversion is not occurring under the conditions used in this study, as has been noted for O2 structures previously.[9] To investigate this further, xrd patterns of the powder and a fresh $Li_xNi_{0.11}Mn_{0.89}O_{2.05}$ electrode, where $x \approx 0.6$, were compared to one that had been cycled 34 times and stopped in approximately the same state-of-charge (Figure 12). Peaks assigned to O2 and O3 structures are retained in the cycled electrode. Significantly, there is no new peak near 32.9º (d=2.71) attributable to

the 103 reflection of a tetragonal spinel, the most likely product of phase conversion at this state-of-charge.

It appears that the ^{7}Li MAS NMR spectrum of a $Li_xAl_{0.11}Mn_{0.89}O_{2.05}$ electrode cycled 62 times does not contain the resonance at 120 ppm attributable to Li in an O3 environment (Figure 13), although the O2 environment is retained. The lack of the resonance at 120 ppm suggests that lithium is gradually removed from O3 environments during prolonged cycling. Note that the resonance for the Li cations in the O2 environment is seen at lower frequency (570 ppm) compared to the fresh electrode due to a slightly more reduced state of the electrode cycled 62 times. A narrow resonance at 500 ppm due to the formation of the stoichiometric spinel was observed in $Li_xM_yO_2$ ($x\approx0.6$, $0.9\leq y\leq1$, O3 structure) after several electrochemical cycles.[27] Due to the broad linewidth of the resonance at 570 ppm, any additional resonance nearby would not be distinguishable. Nevertheless, it appears that no new peak attributable to Li in a cubic (and/or tetragonal) spinel environment with a significant amount is observed in our $Li_xAl_{0.11}Mn_{0.89}O_{2.05}$ electrode.

The phase stability of the O2/O3 structures during cycling under these conditions is notable, given the much-reported propensity of layered manganese oxide with O3 or O'3 structures to convert to spinel rapidly after deep charging. It is not, at present, clear whether this can be attributed to the different stacking arrangement of the O2 layers, which may "pin" the O3 components in place, or because it is not possible to fully extract alkali metal ions upon charge. (The association of O2 stacking in manganese oxides with defects in the transition metal layers may mean that the structure and incomplete removal of ions are related, as we speculated above). These results, however, suggest that it might

be possible to design an electrode with an acceptable compromise between the phase stability of the O2 structure and the higher capacity (or better rate capability) of O3 compounds by manipulating the relative amounts and distributions of these two phases in intergrowth structures. We are currently investigating this possibility using Al and Ni-substituted layered manganese oxides.

IV. Conclusions

Layered substituted manganese oxides with O2 and O2/O3 intergrowth structures were prepared from sodium-containing P2 and P2/P3 precursors. Neither O2 nor O2/O3 electrodes convert to spinel upon cycling in lithium cell configurations, but the latter have higher capacities and better intercalation kinetics than the former. The possibility of designing phase stable, high capacity layered manganese oxide electrodes with intergrowth structures is discussed.

Acknowledgments

This work was supported by the Assistant Secretary for Energy Efficiency and Renewable Energy, Office of FreedomCAR and Vehicle Technologies of the U.S. Department of Energy under Contract No. DE-AC03-76SF00098. T.A. Eriksson was funded by The Hans Werthen Foundation and The American-Scandinavian Foundation.

References

[1] Winter, M; Besenhard, J.O.; Spahr, M.E.; Novak, P. *Adv. Mater.* **1998**, *10*, 725.

[2] Tarascon, J.M.; Armand, M. *Nature* **2001**, *414*, 359.

[3] Blyr, A.; Sigala, C.; Amatucci, G.; Guyomard, D.; Chabre, Y.; Tarascon, J-M. *J. Electrochem. Soc.* **1998**, *145*, 194.

[4] Du Pasquier, A.; Blyr, A.; Courjal, P.; Larcher, D.; Amatucci, G.; Gerand, B.; Tarascon, J-M. *J. Electrochem. Soc.* **1999**, *146*, 428.

[5] Armstrong, A.R.; Bruce, P.G. *Nature* **1996**, *381*, 499.

[6] Ammundsen, B; Paulsen, J. *Adv. Mater.* **2001**, *13*, 943.

[7] Robertson, A.D.; Armstrong, A.R.; Bruce, P.G. *Chem. Mater.* **2001**, *13*, 2380.

[8] Chiang, Y-M.; Sadoway, D.R.; Jang, Y-I.; Huang, B.; Wang, H.; *Electrochem. Solid-State Lett.* **1999**, *2*, 107.

[9] Paulsen, J.M.; Thomas, C.L.; Dahn, J.R. *J. Electrochem. Soc.* **1999**, *146*, 3560.

[10] Shaju, K.M.; Subba Rao, G.V.; Chowdari, B.V.R. *Electrochem. Commun.* **2002**, *4*, 633.

[11] Paulsen, J.M.; Donaberger, R.A.; Dahn, J.R. *Chem. Mater.* **2000**, *12*, 2257.

[12] Paulsen, J.M.; Dahn, J.R. *J. Electrochem. Soc.* **2000**, *147*, 2478.

[13] Lu, Z.; Donaberger, R.A.; Thomas, C.L.; Dahn, J.R. *J. Electrochem. Soc.* **2002**, *149*, A1083.

[14] Lu, Z.; Dahn, J.R. *J. Electrochem. Soc.* **2001**, *148*, A710.

[15] Chick, L.A.; Pederson, L.R.; Maupin, G.D.; Bates, J.L.; Thomas, L.E.; Exarhos, G.J. *Mater. Letters* **1990**, *10*, 6.

[16] Pederson, L.R.; Chick, L.A.; Exarhos, G.J. US Patent 5 114 702, 1992.

[17] Robertson, A.D.; Armstrong, A.R.; Bruce, P.G. *J. Chem. Soc., Chem. Commun.* **2000**, 1997.

[18] Parant, J-P.; Olazcuaga, R.; Devalette, M.; Fouassier, C.; Hagenmuller, P. *J. Solid State Chem.* **1971**, *3*, 1.

[19] Armstrong, A.R.; Paterson, A.J.; Robertson, A.D.; Bruce, P.G. *Chem. Mater.* **2002**, *14*, 710.

[20] Lu, Z.; Donaberger, R.A.; Dahn, J.R. *Chem. Mater.* **2000**, *12*, 3583.

[21] M. Dollé, J. Hollingsworth, T. J. Richardson, and M. M. Doeff, unpublished results.

[22] Lu, Z.; Dahn, J.R. *Chem. Mater.* **2001**, *13*, 1252.

[23] Paulsen, J. M.; Thomas, C. L.; Dahn, J. R. *J. Electrochem. Soc.* **2000**, *147*, 861.

[24] Lee, Y. J.; Wang, F.; Grey, C. P. *J. Am. Chem. Soc.* **1998**, 120, 12601.

[25] Mustarelli, P.; Massarotti, V.; Bini, M.; Capsoni, D. *Phys. Rev. B* **1997**, 55, 12018.

[26] Carlier, D.; Ménétrier, M.; Delmas, C. *J. Mater. Chem*. **2001**, 11, 594.

[27] Armstrong, A. R.; Paterson, A. J.; Bruce, P. G.; Grey, C. P.; Paik, Y. 11th IMLB Conference, 2002, Monterey, California.

[28] Lee, Y. J.; Eng, C.; Grey, C. P. *J. Electrochem. Soc*. **2001**, 148, A249.

[29] Lee, Y. J.; Park, S.-H.; Eng, C.; Parise, J. B.; Grey, C. P. *Chem. Mater*. **2002**, 14, 194.

[30] Eriksson, T.A.; Doeff, M.M. *J. Power Sources*, in press.

Table 1. Unit Cell Parameters of $Na_{0.63}Mn_{0.89}M_{0.11}O_{2.05}$ compounds.

	P2 (space group $P6_3mmc$)		P3 (space group R3M)		Vol. % P2[a]
M	a, Å	c, Å	a, Å	c, Å	
Mn	2.87	11.17			~100
Zn	2.8786(3)	11,185(3)			~100
Cu					~100
Fe	2.8775(5)	11.172(4)			~100
Li	2.85	11.13	2.85	16.83	~65
Co	2.8524(3)	11.161(3)	2.85	16.72	~94
Ni	2.8688(4)	11.197(3)	2.87	16.77	~95
Al	2.8548(5)	11.175(5)	2.85	16.70	~65

a) estimated.

Table 2. Ionic radii of elements, assuming the coordination number 6.[1]

Ion	Ionic radii for various oxidation states (pm)			
	+1	+2	+3	+4
Mn		83	58	53
Zn		74		
Cu	77	73		
Fe		61	55	
Li	76			
Co		65	55	
Ni		69	56	
Al			54	

[1] *CRC Handbook of Chemistry and Physics*, 82nd edition, D.R. Lide, Ed., CRC Press, Boca Raton, FL, USA, 2001.

Table 3. Unit cell parameters of O2 components of ion-exchanged compounds. [a]

M	a, Å	c, Å
Mn	2.84	9.86
Zn	2.833(1)	9.642(9)
Fe	2.842(1)	9.47(1)
Co	2.826(1)	9.61(1)
Ni	2.8393(7)	9.513(6)
Al	2.8328(9)	9.647(8)

a) Space group $P6_3mc$. O3 components not refined.

Figure Captions

Figure 1. a) O'3 structure of α-$NaMnO_2$ and $LiMnO_2$ made by ion-exchanging α-$NaMnO_2$, b) P2 structure of $Na_{0.7}MnO_{2+y}$, c) O2 structure of Li_xMnO_{2+y} made by ion-exchanging P2 $Na_{0.7}MnO_{2+y}$, d) P3 structure of $Na_{0.5}Mn_xM_{1-x}O_2$ and e) O3 structure of $Li_{0.5}Mn_xM_{1-x}O_2$. Alkali metal ion layers are shaded gray, transition metal layers are white and unit cell outlines are shown by dark gray lines.

Figure 2. Scanning electron micrographs of $Li_xMn_{0.89}Cu_{0.11}O_{2.05}$ at two different magnifications.

Figure 3. XRD patterns of $Na_{0.63}Mn_{0.89}M_{0.11}O_{2.05}$ compounds (M = Mn, Zn, Cu, Fe, Li, Co, Ni and Al) and calculated pattern of P2 $Na_{0.66}Ni_{0.33}Mn_{0.67}O_2$ (bottom).

Figure 4. Detail of xrd patterns for $Na_{0.63}Mn_{0.89}M_{0.11}O_{2.05}$ compounds with M=Li, Co, Ni, and Al. Peaks that could be indexed to the P3 structure are marked with an asterisk (*).

Figure 5. (a) Bright-field electron micrograph showing a grain containing coexisted P2 and P3 phase slabs. The common **c**-direction is marked. (b) $[10\bar{1}0]^*$ zone-axis selected-area electron diffraction pattern taken from the dual-phase grain in (a). The common $[000l]^*$ axis is marked, and the diffraction rows arising from P2 and P3 phases, respectively, are indicated.

Figure 6. XRD pattern of $Na_{0.63}Mn_{0.89}Zn_{0.11}O_{2.05}$ before sample was thoroughly dried, showing peaks attributable to a hydrate phase with larger unit cell parameters.

Figure 7. XRD patterns of substituted ion-exchanged compounds, and calculated patterns for O2 Li_xMnO_{2+y} (bottom) and O3 Li_xMnO_2 (second from bottom).

Figure 8. ^{7}Li MAS NMR spectra of $Li_xM_{0.11}Mn_{0.89}O_{2.05}$, where M is (a) Cu, (b) Zn, (c) Ni, (d) Co, (e) Fe, and (f) Al. (g) represents the spectrum of $Na_yLi_{0.11}Mn_{0.89}O_{2.05.}$ The spectra were acquired at a spinning speed of 22.5 kHz. The experiments were performed at room temperature and no attempt was made to control the temperature increase caused by the frictional heat due to magic angle spinning. Spectra are plotted on an absolute intensity scale, taking into account of the number of acquisitions and the sample mass. The isotropic resonances are marked on the spectra; all other peaks are spinning sidebands.

Figure 9. Discharges at 0.05 mA/cm^2 of Li/1M $LiPF_6$ EC-DMC/$Li_xM_{0.11}Mn_{0.89}O_{2.05}$ (M = Mn, Fe, Zn, and Cu) cells between 2.0 and 4.2 V. Cycle numbers are indicated on the graphs.

Figure 10. Discharges at 0.05 mA/cm^2 of Li/1M $LiPF_6$ EC-DMC/$Li_xM_{0.11}Mn_{0.89}O_{2.05}$ (M = Ni, Al, Co) cells between 2.0 and 4.2 V and a Li/1M $LiPF_6$ EC-DMC/$Li_xAl_{0.11}Mn_{0.89}O_{2+y}$ cell between 2.0 and 4.6 V (second from top). Cycle numbers are indicated on the graphs.

Figure 11. Discharges of a Li/1M $LiPF_6$ EC-DMC/$Li_xFe_{0.11}Mn_{0.89}O_{2.05}$ cell at 0.015 mA/cm^2 (—), 0.033 mA/cm^2 (----), and 0.05 mA/cm^2 (···).

Figure 12. XRD patterns of $Li_xNi_{0.11}Mn_{0.89}O_{2.05}$ powder (bottom), fresh electrode (middle), and electrode cycled 34 times (top). Peaks attributable to graphite (used as a conductive additive in the electrode) are marked with a ■ and those attributable to the aluminum current collector are marked with a ●.

Figure 13. ^7Li MAS NMR spectra of a $Li_xAl_{0.11}Mn_{0.89}O_{2.05}$ electrode (a) before and (b) after 62 cycles (OCV=3.12 V). The spectra were acquired at a spinning speed of 22 kHz. The other conditions are the same as those described in figure 8.

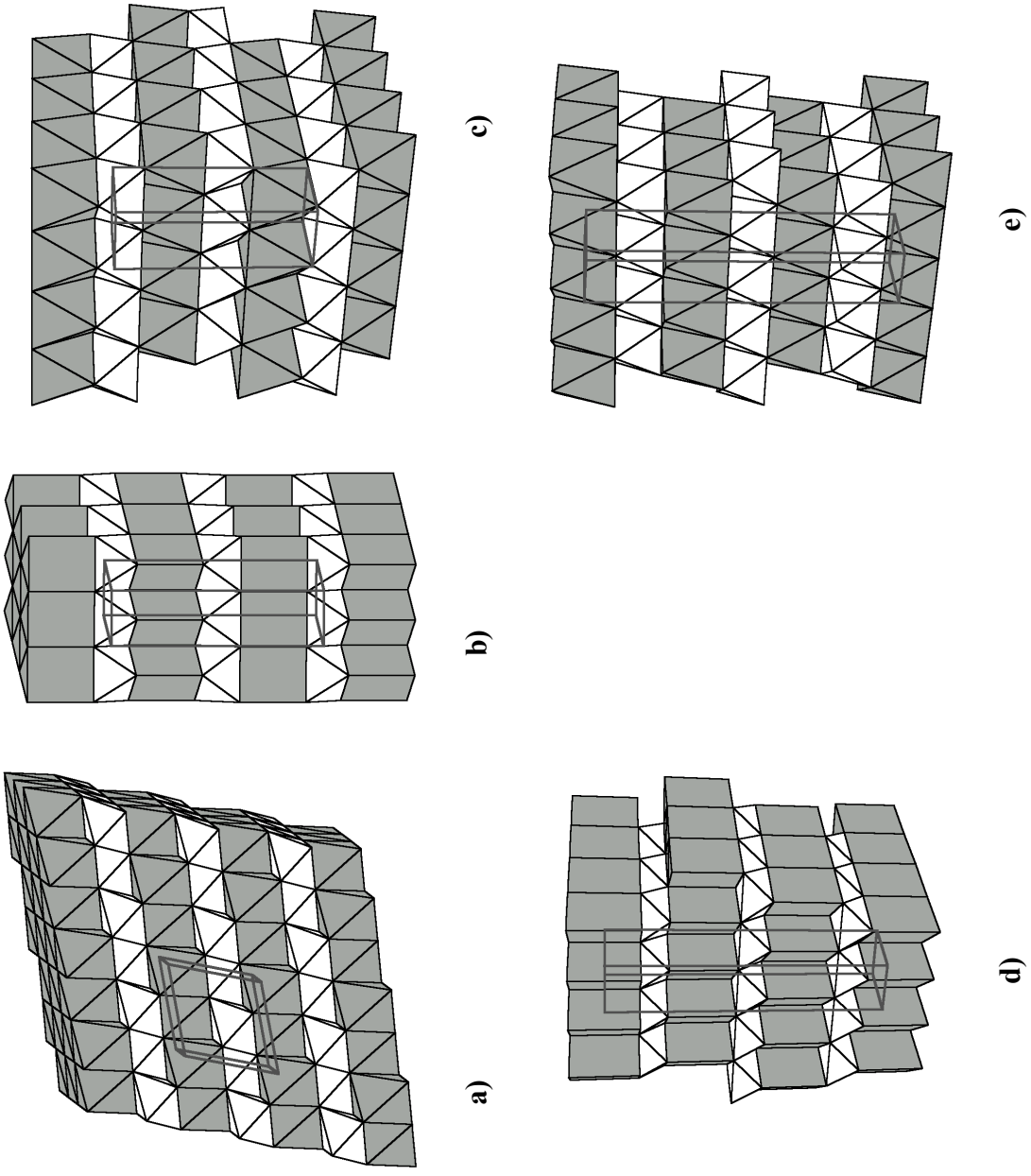

Eriksson et al., “Influence of Substitution…”, Figure 1

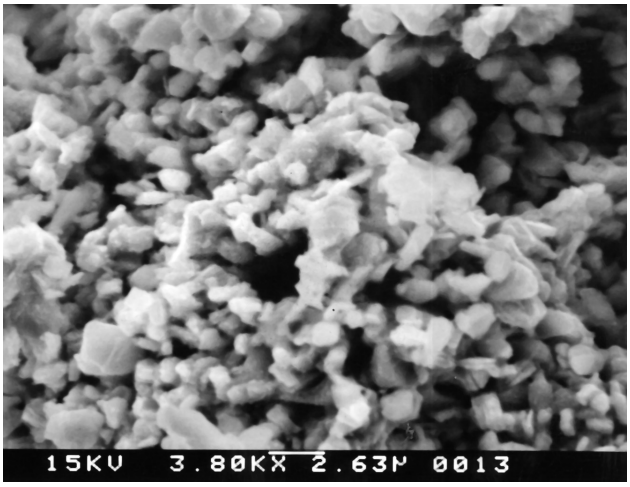

(a)

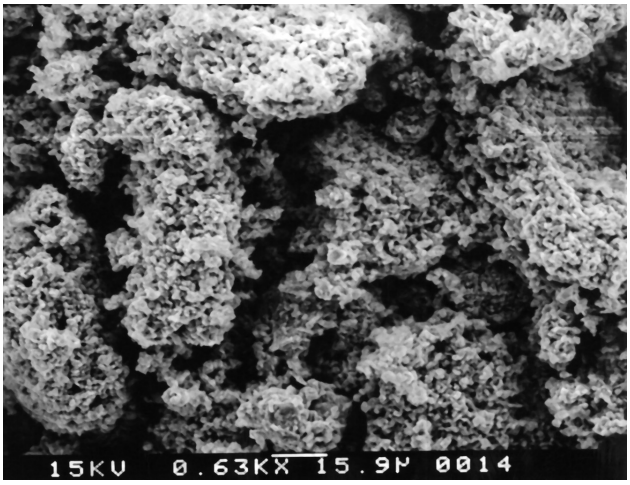

(b)

Eriksson et al., “Influence of Substitution…” Figure 2

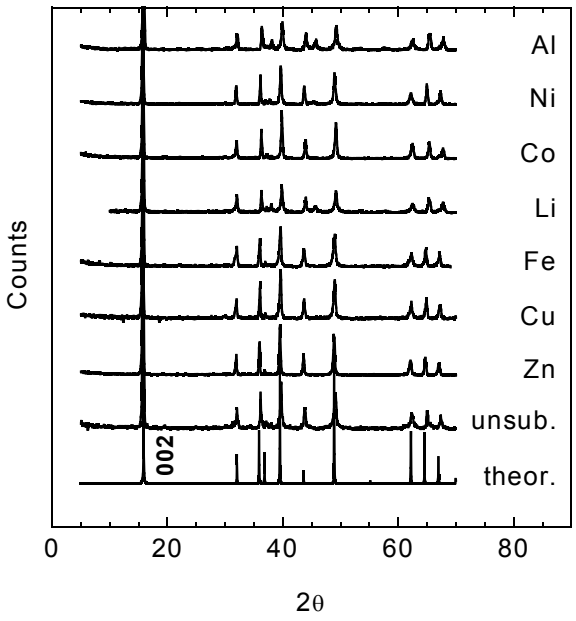

Eriksson et al, “Influence of Substitution…” Figure 3

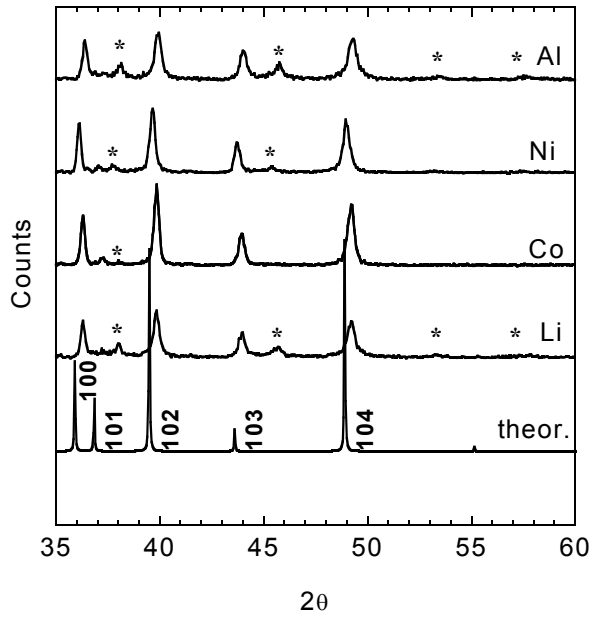

Eriksson et al., “Influence of Substitution….” Figure 4

(a)

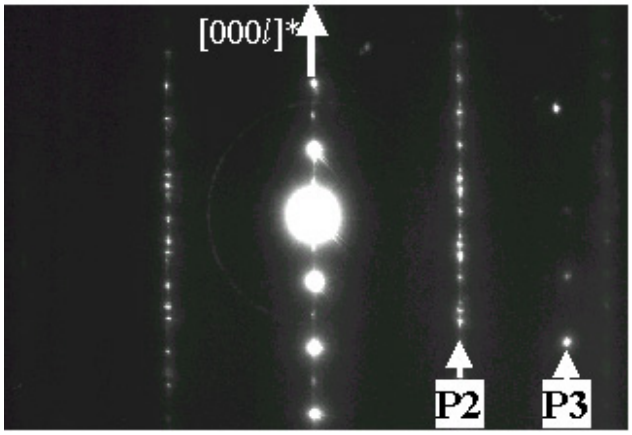

(b)

Eriksson et al., “Influence of Substitution…” Figure 5

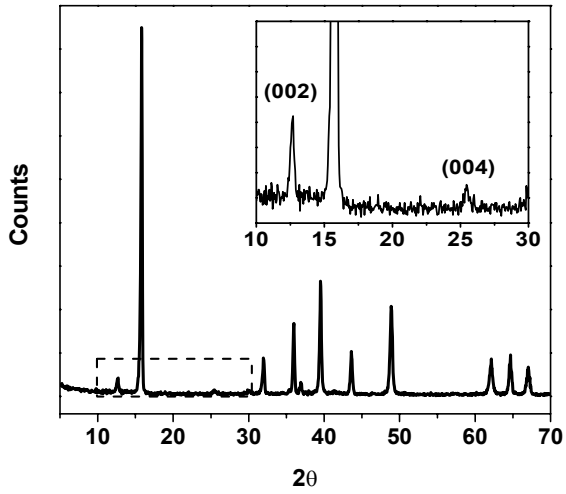

Eriksson et al., “Influence of Substitution…” Figure 6

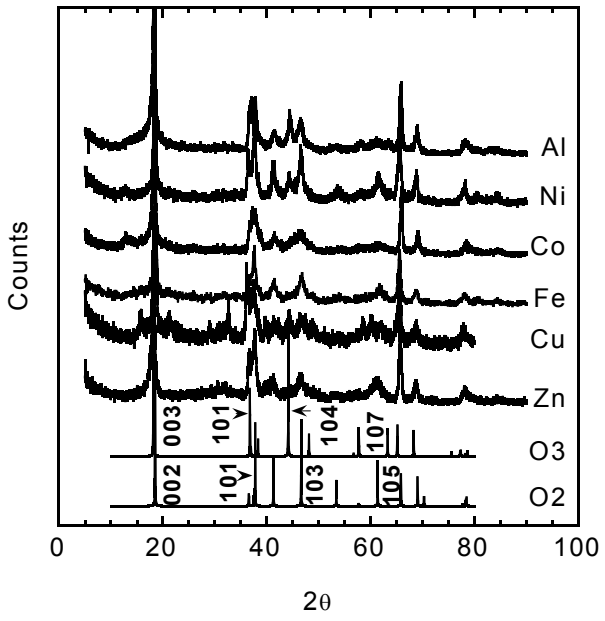

Eriksson et al., "Influence of Substitution…" Figure 7.

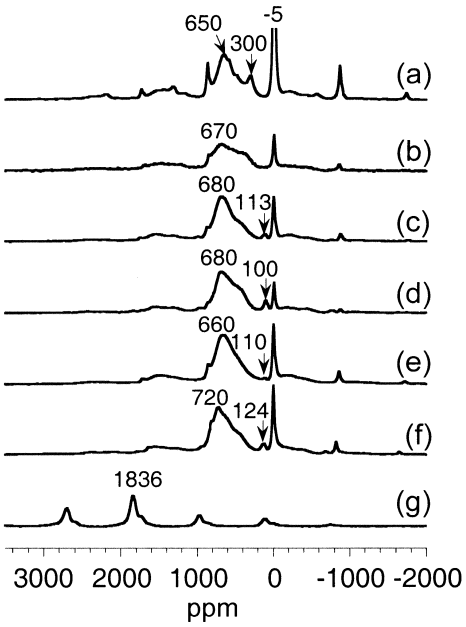

Eriksson et al., “Influence of Substitution…” Figure 8

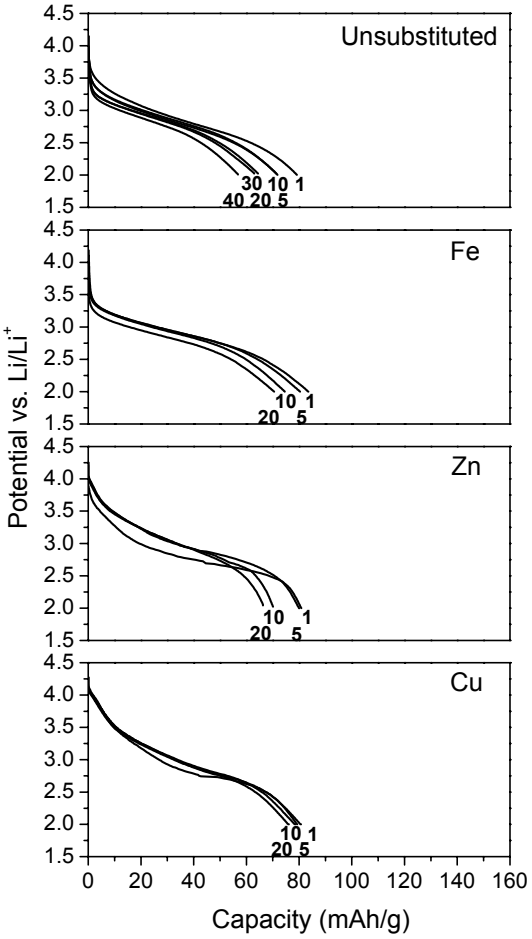

Eriksson et al., “Influence of Substitution…” Figure 9

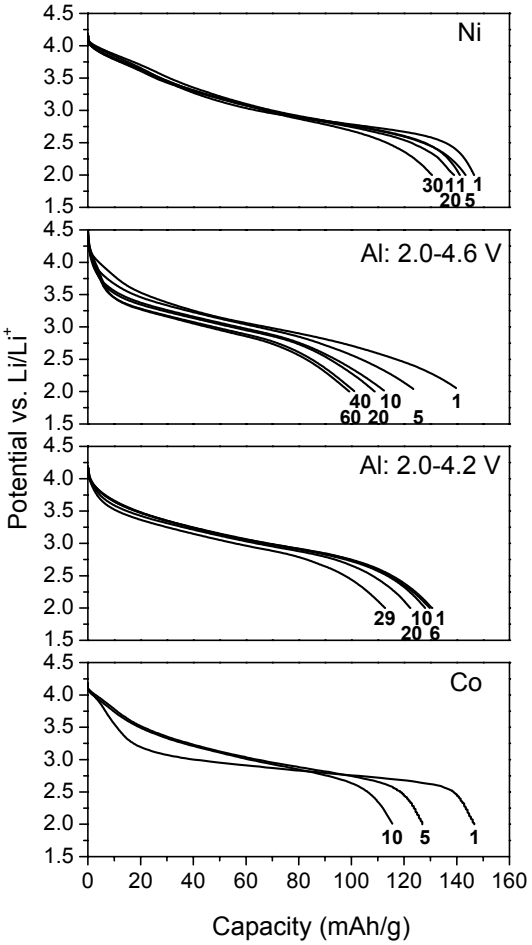

Eriksson et al., "Influence of Substitution…" Figure 10.

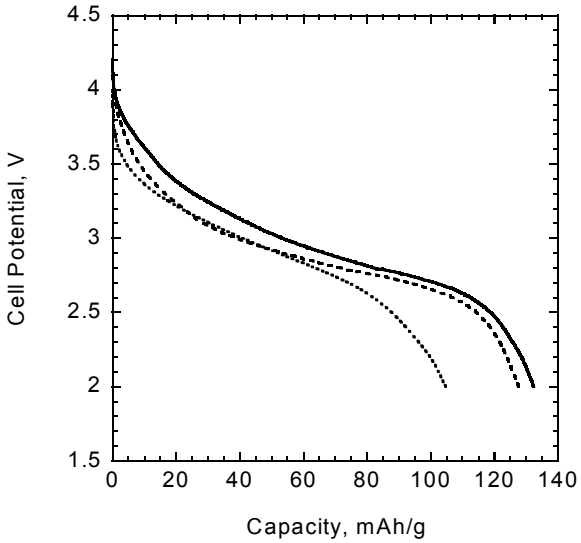

Eriksson et al., “Influence of Substitution…” Figure 11

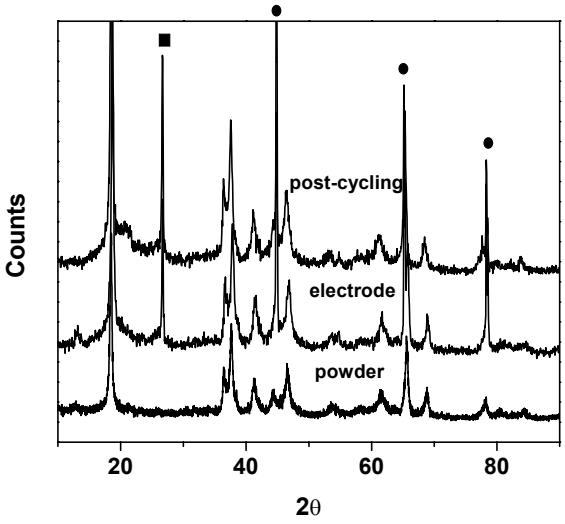

Eriksson et al., “Influence of Substitution…” Figure 12

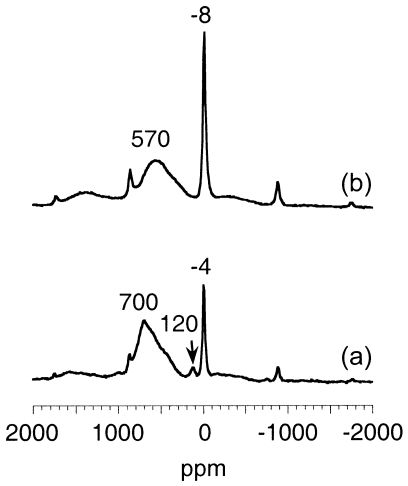

Eriksson et al., “Influence of Substitution…” Figure 13